JOURNAL OF PROPULSION AND POWER
Vol. 23, No. 5, September–October 2007

Analytical Ion Thruster Discharge Performance Model

Dan M. Goebel,* Richard E. Wirz,† and Ira Katz‡
Jet Propulsion Laboratory, California Institute of Technology, Pasadena, California 91109

DOI: 10.2514/1.26404

A particle and energy balance model of the plasma discharge in magnetic ring-cusp ion thrusters has been developed. The model follows prior work in the development of global zero-dimensional discharge models that use conservation of particles into and out of the thruster, conservation of energy into the discharge and out of the plasma in the form of charged particles to the walls and beam, and plasma radiation. The present model is significantly expanded over the prior art by closing the set of equations with self-consistent calculations of the internal neutral pressure, electron temperature, primary electron density, electrostatic ion confinement (due to the ring-cusp fields), plasma potential, discharge stability, and time-dependent behavior during recycling. The model only requires information on the thruster geometry, ion optics performance, and electrical inputs, such as discharge voltage and currents, to produce accurate performance curves of discharge loss vs mass utilization efficiency. The model has been benchmarked against several ion thrusters, and successfully predicts the thruster discharge loss as a function of mass utilization efficiency for a variety of thrusters. The discharge performance model will be described and results showing ion thruster performance and stability presented.

Nomenclature

A = area
A_a = plasma electron loss area
A_{as} = anode surface area
A_p = primary electron loss area
A_g = grid area
B = magnetic field strength
C = neutral gas conductance of grids
E = electric field in the plasma
e = electron charge
f_c = ion confinement factor
I_a = plasma electron current to the anode
I_i = ion current
I_{ia} = ion current to the anode
I_e = discharge cathode emission current
I_B = beam current
I_p = total ion production
I_d = discharge current
I_k = ion current backflowing to cathode
I_L = primary current lost to anode
I_s = ion current to the screen grid
I^+ = excited neutral production
I_{sp} = specific impulse
k = Boltzman's constant
L = primary electron path length
L_c = total cusp length
l = diffusion length
M = ion mass
m = electron mass
n_e = electron density
n_i = ion density
n_o = neutral density
n_p = primary density
P = electron loss probability
P_o = neutral pressure
Q = neutral flow rate
r_e = electron Larmor radius
r_h = hybrid radius
r_i = ion Larmor radius
r_p = primary Larmor radius
T = effective grid transparency
T_a = grid optical transparency
T_e = electron temperature
T_o = neutral gas temperature
U^+ = xenon ionization potential
U^* = xenon excitation potential
V_c = hollow cathode voltage drop
V_D = discharge voltage
V_k = primary electron energy
V_p = potential drop in plasma
V = plasma volume
v = velocity
v_a = ion acoustic velocity
v_p = primary velocity
η_c = Clausing factor
η_D = discharge loss
η_m = mass utilization efficiency
μ_e = electron mobility
ν_{en} = electron-neutral collision frequency
ν_{ei} = electron-ion collision frequency
ν = ratio of ν_{en} to ν_{ei}
σ = collision cross section
σ_i = ionization cross section
σ^* = excitation cross section
τ_c = primary collision time
τ_g = neutral gas time constant of chamber
τ_p = primary confinement time
τ_t = total thermalization time
ϕ = plasma potential relative to anode

Presented as Paper 4486 at the 42nd AIAA/ASME/SAE/ASEE Joint Propulsion Conference & Exhibit, Sacramento, California, 9–12 July 2006; received 8 July 2006; revision received 5 February 2007; accepted for publication 7 February 2007.

*Senior Research Scientist, Advanced Propulsion Group, Jet Propulsion Laboratory. Senior Member AIAA.
†Senior Engineer, Advanced Propulsion Group, Jet Propulsion Laboratory. Member AIAA.
‡Group Supervisor, Advanced Propulsion Group, Jet Propulsion Laboratory. Member AIAA.

I. Introduction

ION thrusters require efficient ionization of propellant atoms, which can be accomplished by a variety of plasma generation methods. These include DC electron discharges, RF and microwave

discharges, and arc-plasma discharges. Ion thrusters that use electron discharges to produce the plasma, often called electron bombardment thrusters, have been flown on a NASA mission [1] and are now routinely used for station keeping on geosynchronous communications satellites [2]. Models of the discharge chamber performance in ion thrusters have been described in the literature for many years [3–6], but these models have been largely empirical and require detailed measurements of plasma parameters or thruster performance. Brophy developed the first comprehensive discharge chamber model [7] in the 1980s for ring-cusp magnetic confinement, electron bombardment thrusters based on particle and energy balance in the discharge chamber. This model assumed a uniform plasma and used volume-averaged ionization and excitation rates, and therefore has been called a "0-D model." Brophy's model required measurements of some parameters in the thruster or data from plasma and gas flow simulations to accurately predict the thruster behavior. An improved version of this model was developed [8] with plasma potential and discharge stability effects [9], and was used to predict the performance of the Nuclear Electric Xenon Ion System (NEXIS) thruster [10,11]. This model still also required some plasma parameter inputs (such as electron temperature), and so was not a completely predictive tool.

Based on this previous work, a completely self-consistent analytical plasma discharge model has been developed for ring-cusp ion thrusters. The model requires only the mechanical configuration, the grid transparency from an ion optic code, the hollow cathode voltage drop, and electrical inputs to the discharge chamber to self-consistently calculate the neutral gas pressure, electron temperature, primary density, ion and electron confinement, and plasma potential required to produce curves of discharge loss as a function of mass utilization efficiency. In addition, the model determines the plasma discharge stability for the discharge chamber size and magnetic field configuration, and explains the discharge behavior observed during recycling and turn on. These features make the 0-D ion thruster discharge chamber model predictive, which aides in the understanding of the discharge chamber performance for different thruster configurations. The 0-D model naturally does not address spatial nonuniformities, and so is best applied to fairly uniform plasma thrusters. However, the model still works well for hollow cathode discharges where the electrons from the localized electron source apparently disperse in the largely collisionless plasma and neutral densities, and the system is dominated by the average volume effects. The fully self-consistent model will be described and examples of its results presented.

II. Ion Thruster Design

Ion thrusters with a DC electron discharge plasma generator use a hollow cathode electron source and an anode potential discharge chamber with magnetic multipole boundaries to improve the ionization efficiency and generate the plasma. Ions are extracted from this plasma and accelerated by grids to form an ion beam and produce thrust at high specific impulse I_{sp}. An illustration of an electron bombardment ion thruster [10] is shown in Fig. 1. The four major components of the thruster are apparent: 1) discharge hollow cathode, 2) discharge chamber, 3) accelerator electrodes, and 4) neutralizer hollow cathode.

Electrons extracted from the hollow cathode enter the discharge chamber and ionize the injected propellant gas. Magnetic fields applied in the discharge chamber provide confinement primarily of the energetic electrons, which increases the electron path length before being lost to the anode wall and improves the ionization efficiency. The ion thruster schematic in Fig. 1 shows an example of a ring-cusp thruster design with alternating magnetization rings of permanent magnets positioned around the thruster axis that produce a multipole magnetic field for plasma confinement. Proper design of the magnetic field is critical to providing sufficient confinement to improve efficiency and adequate electron loss to produce stable discharges over the operation range of the thruster. Either two or three electrically biased grids at the thruster exit accelerate the ions to form the thrust beam. Finally, a hollow cathode electron emitter is

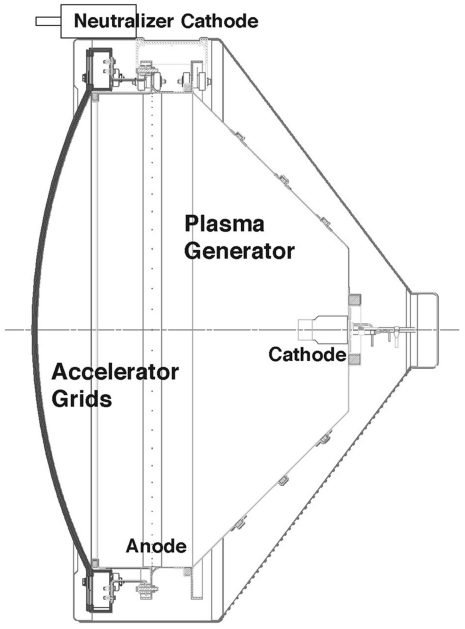

Fig. 1 Illustration of an electron bombardment ion thruster.

positioned outside the thruster body to provide electrons to neutralize the ion beam and maintain the potential of the thruster and spacecraft relative to the space plasma potential.

Several power supplies are required to operate the cathodes, electron discharge, and accelerator in ion thrusters. A simplified electrical schematic typically used for ion thrusters is shown in Fig. 2. The cathode heater and keeper supplies are not shown in this figure. The discharge supply is connected between the hollow cathode and the anode, and is normally run in the current regulated mode to provide stable discharges from the hollow cathode. The first grid, called the screen electrode, is normally connected to cathode potential to provide some electrostatic confinement of the electrons in the discharge. Ions that penetrate the apertures in this grid are accelerated by the potential applied between the screen grid

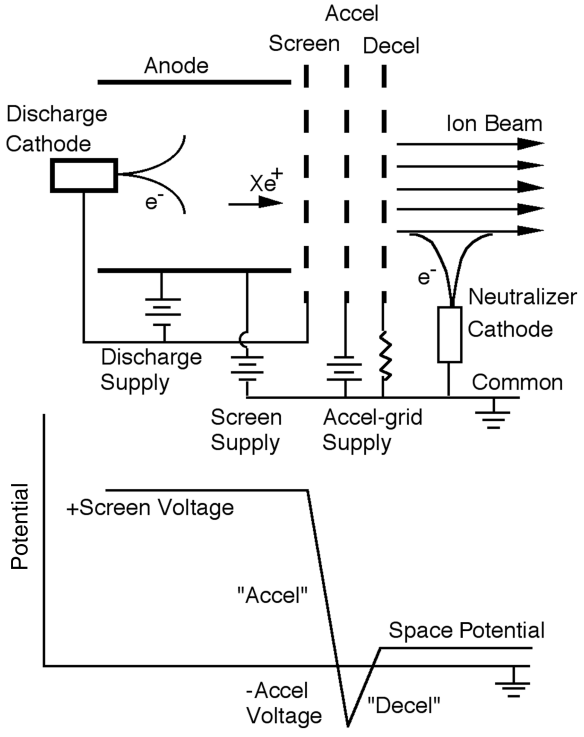

Fig. 2 Electrical schematic of the ion thruster without the cathode heater and keeper supplies.

and the second grid, which is called the accelerator (or accel) grid. The high-voltage bias is connected between the anode and the common of the system, which is normally connected to the neutralizer cathode and called neutralizer common. The accel grid is biased negative relative to the neutralizer common to prevent the very mobile electrons in the beam plasma from backstreaming into the thruster and overloading the screen supply. The ion beam is both charge and density neutralized by electrons from the neutralizer cathode, which self-biases the neutralizer common potential sufficiently negative relative to the space potential to produce the required number of electrons to neutralize the beam.

In Fig. 2, a three-grid system is shown in which a final grid called the "decel grid" is placed downstream of the accel grid. This grid shields the accel grid from ion bombardment from charge-exchanged produced ions in the beam backflowing toward the thruster, and eliminates downstream "pits and grooves erosion" observed in two-grid systems. Three-grid systems therefore have longer accel grid life than two-grid systems, and also generate less sputtered material into the plume that can impact the spacecraft. These benefits are traded against the added complexity of positioning and aligning a third grid. Three-grid systems are used on the Xenon Ion Propulsion System (XIPS) ion thrusters [2].

Empirical studies over the past 50 years have investigated the optimal design of the magnetic field to confine the electrons and ions in the thruster. At this time, only two magnetic field geometries are still used in dc ion thrusters: the multipole magnetic field ring-cusp thrusters and the divergent solenoidal magnetic fields in Kaufman-type thrusters. In ring-cusp thrusters, the number of rings is optimized for different size thrusters [8]. These types of thrusters provide surface magnetic confinement of the electrons with finite loss at the magnetic cusps, and electrostatic confinement of the ions from the anode wall due to the quasi-ambipolar potentials at the boundary caused by the transverse magnetic field. Line-cusp thrusters use a similar geometry but the cusps run axially along the chamber wall. Asymmetries at the ends of the line cusps cause plasma losses and difficulties in producing a uniform symmetric field at the cathode exit, which adversely affects the electron confinement and thruster efficiency. The 0-D model described in this paper is therefore applied to ring-cusp magnetic designs.

III. 0-D Ion Thruster Model

The complete particle flows in a thruster discharge chamber are shown in Fig. 3. The primary electron current emitted by the discharge hollow cathode I_e generates ions and plasma electrons. The ions flow to the screen grid I_s, to the anode wall I_{ia}, back to the cathode I_k, and become beam ions I_B. Some fraction of the primary electrons is lost directly to the anode at the magnetic cusps I_L. The plasma electrons are also lost to the anode at the cusps I_a, with only a very small fraction lost transverse to the magnetic field between the cusps corresponding to the ambipolar current flows in this region.

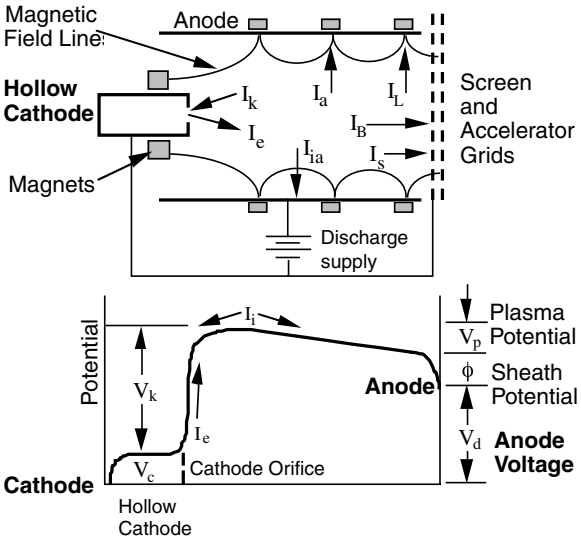

Fig. 3 Schematic of thruster showing particle flows and potential distribution in the discharge chamber.

The particle energies are determined by the potential distribution in the thruster. Figure 3 also schematically shows the potential in the plasma chamber. Electrons from the plasma inside the hollow cathode are extracted through the orifice and into the discharge chamber where they gain the energy $V_k = V_d - V_c + V_p + \phi$. These electrons represent the source of the primary electron population observed in thrusters [12,13] as a peak in the tail of the bulk Maxwellian distribution of electrons. Some of these electrons cause ionization near the hollow cathode output, which produces a higher plasma density locally near the cathode exit that must be dispersed before reaching the grid region to produce a uniform plasma profile across the grids. The potential drop in the plasma V_p can be approximated by $T_e/2$ due to the required presheath potential to obtain the Bohm velocity. Primary electrons that find the cusps and electrons in the tail of the Maxwellian distribution that overcome the anode sheath are collected by the anode at the cusps.

The 0-D model is used to calculate discharge loss as a function of the mass utilization efficiency, which is useful in plotting the discharge chamber performance curves that best characterize the discharge chamber behavior. The 0-D model is constructed as follows. The particle flows and potential distribution in the thruster are shown schematically in Fig. 3. Monoenergetic primary electrons with a current I_e are assumed emitted from the hollow cathode orifice into the discharge chamber, where they ionize the background gas to produce a fairly uniform plasma. Electrons produced in the ionization process and thermalized primaries create a Maxwellian plasma electron population, the tail of which can also ionize the neutral gas. Because of the relatively high magnetic field produced by the magnets near the wall, the electron Larmor radius is much smaller than the dimensions of the discharge chamber and the primary and plasma electrons are lost only at the magnetic cusp where the magnetic field lines are essentially perpendicular to the surface. Ions produced in the discharge chamber can flow back to the hollow cathode, to the anode wall or to the plane of the accelerator. At the accelerator, these ions are either intercepted and collected by the screen electrode with an effective transparency T, or enter the grids to become beam ions. The screen-grid transparency depends on the optical transparency of the grid and the penetration of the high voltage fields from the accelerator region into the screen apertures. This transparency is calculated by ion optics codes, and is an input to the discharge model.

In this model, the high voltage power supply that accelerates the ions, called the screen supply, is connected to the anode. This means that the ions fall from the average plasma potential in the discharge chamber and form the beam. It is also possible to connect the screen supply to the screen and cathode, which means that the ion current in the beam must pass through the discharge supply. This changes the algebra slightly in calculating the discharge performance, but not the results. The components of particle and energy balance model are as follows.

A. Ion and Excited Neutral Production Rates

Ions are produced by both the primary electrons and by the tail of the Maxwellian distribution of the plasma electrons. The total number of ions produced in the discharge is given by

$$I_p = n_o n_e \langle \sigma_i v_e \rangle V + n_o n_p \langle \sigma_i v_p \rangle V, \text{ particles/s} \qquad (1)$$

where n_o is the neutral atom density, n_e is the plasma electron density, σ_i is the ionization cross section, v_e is the plasma electron velocity, V is the plasma volume inside the discharge chamber, n_p is the primary electron density, and v_p is the primary electron velocity. The term in the brackets is the ionization cross section averaged over the distribution of electron energies, which is usually called the reaction rate coefficient.

An example of ionization and excitation cross sections [14,15] commonly used for electron impact on xenon is shown in Fig. 4. If it

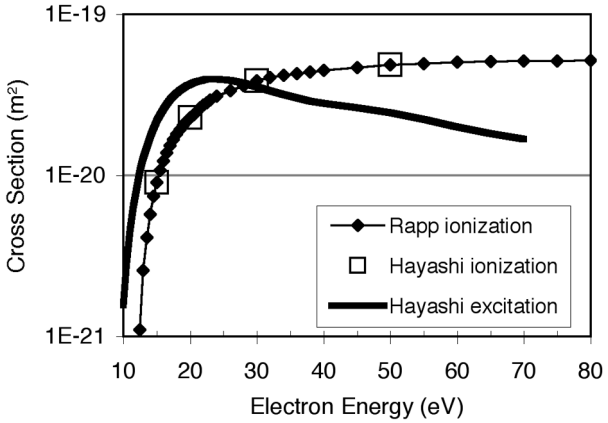

Fig. 4 Xenon ionization and excitation cross sections [14,15].

is assumed that the primary electrons are monoenergetic, then the reaction rate coefficient in Eq. (1) for primary ionization is just the cross section in Fig. 4 times the corresponding primary electron velocity. If the primaries have a distribution in energy, then the cross section must be averaged over the distribution.

Excited neutrals are also produced by both the primary electrons and the tail of the Maxwellian distribution of the plasma electrons. The total number of excited neutrals produced in the discharge is given by

$$I^* = n_o n_e \langle \sigma^* v_e \rangle V + n_o n_p \langle \sigma^* v_p \rangle V, \text{ particles/s} \tag{2}$$

where σ^* is the excitation cross section. Again, the excitation cross section [15] is averaged over the distribution in primary and plasma electron energies to produce the reaction rate coefficients in the brackets.

The reaction rate coefficients calculated by averaging the ionization and excitation cross sections over a Maxwellian energy distribution are shown in Fig. 5. We see that the rate of excitation exceeds that of ionization if the electron temperature is relatively low (below about 9 eV). That means that at low electron temperatures a significant amount of the energy in the discharge goes into excitation of the neutrals at the expense of ionization. This is one of the (many) reasons that the energy cost of producing an ion in ion thrusters is usually well over 10 times the ionization potential.

B. Electron Confinement at the Anode

The primary electrons injected into the discharge chamber from the hollow cathode bounce around the chamber volume until they are either lost directly to the anode wall by finding a cusp, make an ionization or excitation collision, or are thermalized by Coulomb interactions with the plasma electrons. The primary current lost directly to the anode cusps is given by

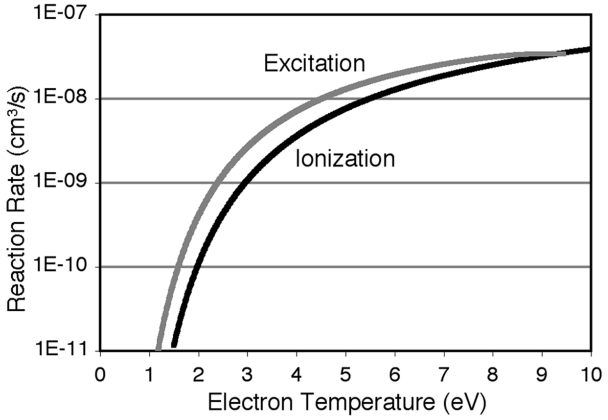

Fig. 5 Xenon ionization and excitation reaction rate coefficients averaged over a Maxwellian electron distribution.

$$I_L = n_p e v_p A_p \tag{3}$$

where n_p is the primary electron density, v_p is the primary electron velocity, and A_p is the loss area for the primaries.

The loss area for primary electrons at the cusp is given by [16]

$$A_p = 2 r_p L_c = \frac{2}{B}\sqrt{\frac{2 m V_{\text{pe}}}{e}} L_c \tag{4}$$

where r_p is the primary electron Larmor radius, B is the magnetic field strength at the cusp at the anode wall, eV_{pe} is the primary electron energy, e is the electron charge, and L_c is the total length of the magnetic cusps (sum of the length of the cusps).

The primary electron confinement time is then

$$\tau_p = \frac{V}{v_p A_p} \tag{5}$$

The mean primary electron path length before finding a cusp and being lost to the wall is $L = v_p \cdot \tau_p$. Likewise, the collision mean free path is $\lambda = 1/n_o\sigma$, where σ represents the total inelastic collision cross section for the primary electrons. The probability that a primary electron will be lost to the anode is then

$$P = [1 - \exp^{-n_o \sigma L}] = [1 - \exp^{(-n_o \sigma V / A_p)}] \tag{6}$$

By providing strong magnetic field strengths at the cusp to minimize the primary loss area, the probability of a primary electron being lost directly to the anode can be made very small. Likewise, ion thrusters with large volumes and/or operated at higher internal neutral gas densities will also reduce primary electron loss to the anode. Minimizing the energy loss associated with primaries being lost before making a collision in this way is required to maximize the efficiency of the thruster.

An example of the probability of a primary making a collision before finding a cusp is shown in Fig. 6 for the case of the NEXIS thruster [10,11] designed with either four or six magnetic cusps. For the design with six cusps, it is required to have cusp field strengths approaching 2000 G at the surface of the anode to ensure that the primaries are not lost prematurely. Designs with a smaller number of ring cusps, corresponding to a smaller primary anode collection area, require less magnetic field strength to achieve the same benefit. However, we will see later that the number of cusps affects efficiency by impacting the anode-loss area for electrons, and that maximizing the probability of a primary making a collision before being lost in Eq. (6) is only one of the tradeoffs in designing an ion thruster.

Because the primary electron current lost directly to the anode is designed to be small for best efficiency, and the ion current is a small fraction of the discharge current, the discharge current is carried to the anode mainly by the plasma electrons. The plasma electrons are also only lost at the magnetic cusps, but their motion is affected by the ions penetrating the cusp and the plasma electrons are lost to a hybrid anode area given by [16]

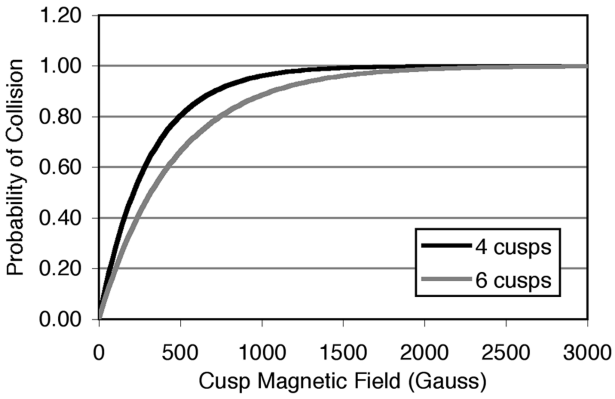

Fig. 6 Probability of primary electron collision before loss at the anode cusps vs cusp field.

$$A_a = 4r_h L_c = 4\sqrt{r_e r_i} L_c \tag{7}$$

where r_h is the hybrid Larmor radius, r_e is the electron Larmor radius, and r_i is the ion Larmor radius. The current of plasma electrons I_a that overcomes the sheath at the anode is

$$I_a = \frac{1}{4}\left(\frac{8kT_e}{\pi m}\right)^{1/2} en_e A_a \exp^{-e\phi/kT_e} \tag{8}$$

where ϕ is the plasma potential relative to the anode (essentially the anode sheath potential).

The plasma in the discharge chamber obeys particle conservation in that the current injected into the volume is the primary electron current, the current lost to the anode is the sum of the direct primary loss, the plasma electron loss, and some ion loss, and the current lost to cathode potential surfaces and the accelerator is the ions that are produced in the discharge. The plasma potential will adjust itself such that the plasma electron current to the anode is equal to the ion current out of the discharge. For a given plasma density and temperature, which determines the random electron flux incident on the sheath, changing the anode area will change the sheath voltage, which affects both the energy loss though the sheath and the stability of the discharge.

C. Ion Confinement at the Anode

Ions are typically unmagnetized in ion thruster discharge chambers because the magnetic field is relatively low everywhere except at the magnetic cusps, which results in a large ion Larmor radius compared with the thruster dimensions. That implies that the current of ions flowing out the plasma volume in any direction is given by the Bohm current [17]:

$$I_i = \frac{1}{2} n_i e \sqrt{\frac{kT_e}{M}} A \tag{9}$$

where n_i is the ion density in the center of the discharge and A is the total ion loss area. For the case of the plasma potential positive relative to the anode, the total ion loss area includes the cusp area A_a where the field lines are perpendicular to the anode surface. However, the magnetized electrons near the anode wall between the cusps influence the ion motion by electrostatic effects, causing ambipolar flows to the walls between the cusps. It is possible to analyze the electron and ion transport across the magnetic field between the cusps and calculate the reduction in the ion velocity caused by the reduced transverse electron drift speed. This can be used to calculate the rate of ion loss to the anode compared with the unmagnetized Bohm current ion loss rate (to the grids).

Ring-cusp thrusters can be designed with various numbers of rings, distances between the rings, and magnet sizes that determine the magnetic field strength in the discharge chamber. The magnetic multipole boundary in ring-cusp structures produces radial and azimuthal components of the magnetic field. Although analytical calculations of the field strength in the multipole structure are possible, it is much more common to use a commercial available two- or three-dimensional magnetic field solver, like the commercial Maxwell three-dimensional code,[§] to find the fields. Figure 7 shows the measured and calculated contours of constant magnetic field strength for an example six-ring-cusp thruster design [10]. The 60 G contour is closed all along the boundary, which will be shown to provide good ion confinement between the cusps.

To evaluate the ion loss across the magnetic field, the steady-state transverse electron equation of motion, including electron-neutral and electron-ion collisions, is given by [18]

[§]Maxwell 3-D is a product of Ansoft Corp., http://www.ansoft.com/products/em/max3d/overview.cfm.

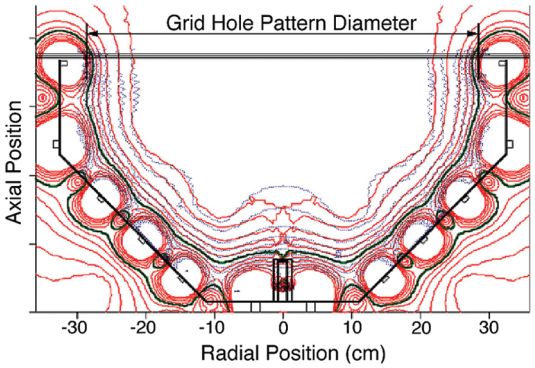

Fig. 7 Measured and calculated magnetic field contours for a ring-cusp thruster discharge chamber [10] using six rings of SmCo magnets.

$$mn\left(\frac{dv_e}{dt} + (v\cdot\nabla)v\right) = -en(E + v_e xB) - kT\nabla n - mnv_{en}(v_e - v_o) - mnv_{ei}(v_e - v_i) = 0 \tag{10}$$

where v_o is the neutral velocity. This equation must be separated into the two transverse velocity components:

$$v_x + \mu_e E + \frac{e}{mv_e} v_y B + \frac{kT}{mv_e}\frac{\nabla n}{n} - \frac{v_{ei}}{v_e} v_i = 0 \tag{11}$$

$$v_y + \mu_e E - \frac{e}{mv_e} v_x B + \frac{kT}{mv_e}\frac{\nabla n}{n} - \frac{v_{ei}}{v_e} v_i = 0 \tag{12}$$

where $v_e = v_{en} + v_{ei}$, $\mu_e = e/mv_e$, and we neglect v_o compared with v_e. Solving for v_y and eliminating the ExB and diagmagnetic drift terms in the v_x direction, the transverse electron velocity is given by

$$v_e\left(1 + \mu_e^2 B^2\right) = \mu_e\left(E + \frac{kT}{e}\frac{\nabla n}{n}\right) + \frac{v_{ei}}{v_e} v_i \tag{13}$$

Assuming ambipolar diffusion, we equate the electron and ion transverse velocities to give

$$v_i = \frac{\mu_e}{\left[1 + \mu_e^2 B^2 - (v_{ei}/v_e)\right]}\left(E + \frac{kT}{e}\frac{\nabla n}{n}\right) \tag{14}$$

The minimum magnetic field to produce an ion velocity v_i is given by

$$B = \frac{v_e m}{e}\sqrt{\frac{e}{mv_e v_i}\left(E + \frac{T_e}{\ell}\right) - \left(\frac{\nu}{1+\nu}\right)} \tag{15}$$

where $\nu = v_{en}/v_{ei}$ and $\nabla p/en = \nabla(nkT_e)/en$ is approximately T_e/l for l representing the length the ions travel radially in the transverse magnetic field between the cusps. The value of l can be estimated from calculations of the transverse magnetic field vs the distance from the wall between the cusps, and is usually on the order of 2–3 cm. Setting $E = 0$ in Eq. (15) gives the case of $v_i = v_{\text{thermal}}$, which essentially cancels out the presheath potential that normally accelerates the ions to the Bohm velocity with the ambipolar electric field from the reduced transverse-mobility electrons. The flux of ions passing through the transverse magnetic field is then reduced, and this smaller ion flux is finally accelerated to the Bohm velocity close to the anode wall to satisfy the sheath criterion. Ions are conserved in this model because ions that are inhibited from flowing to the anode wall due to the transverse fields instead flow axially toward the grids where there is no confinement.

However, it is not necessary to limit this to the case of $E = 0$. If the magnetic field is smaller than the critical B that causes $E = 0$, then the transverse electron mobility increases and a finite electric field exists in the magnetic diffusion length l. The ions fall through whatever potential difference is set up by this electric field, which

means that the ions are accelerated to an energy given by

$$\frac{1}{2}Mv_i^2 = eE \cdot l \tag{16}$$

The transverse magnetic field and ambipolar flow change the electric field magnitude in the presheath region and reduce the acceleration of the ions toward the wall. However, in the limit of no magnetic field, the electric field must accelerate the ions only to the Bohm velocity, which results in a net electric field in the plasma edge-region limited to

$$E = -\frac{mv_i^2}{el} \tag{17}$$

Note that the electric field sign must be negative for the ion flow in this region. Using Eq. (17) in Eq. (15), the minimum magnetic field to produce an ion velocity of v_i is

$$B = \frac{v_e m}{e}\sqrt{\frac{e}{mv_e v_i}\left(\frac{T_e}{\ell} - \frac{Mv_i^2}{e\ell}\right) - \left(\frac{\nu}{1+\nu}\right)} \tag{18}$$

Alternatively, the modified electric field given in Eq. (17) can be can be inserted into Eq. (14) with $\nabla(nkT_e)/en$ again approximately equal to T_e/l to produce an expression for the ion velocity:

$$v_i^2 + \frac{el}{\mu_e M}\left(1 + \mu_e^2 B^2 - \frac{\nu_{\text{ei}}}{\nu_e}\right)v_i - \frac{eT_e}{M} = 0 \tag{19}$$

This quadratic equation can easily be solved for the ion velocity in terms of the transverse magnetic field.

The parameters in the terms $\nu_e = \nu_{\text{en}} + \nu_{\text{ei}}$ and $\nu = \nu_{\text{en}}/\nu_{\text{ei}}$ are given in SI units [19] for xenon as

$$\begin{aligned} \nu_{\text{en}} &= \sigma\sqrt{\frac{8eT_e}{\pi m}}, \qquad \sigma = 6.6\times 10^{-19}\left(\frac{(T_e/4)-0.1}{1+(T_e/4)^{1.6}}\right) \\ \nu_{\text{ei}} &= 2.9\times 10^{-12}\frac{n_e\,\ell_n\,\Lambda}{T_e^{3/2}}, \qquad \ell_n\,\Lambda = 23 - 0.5\,\ell_n\left(\frac{10^{-6}n_e}{T_e^3}\right) \end{aligned} \tag{20}$$

where $\ell_n\,\Lambda$ is the Coulomb logarithm. If we define an ion confinement factor

$$f_c = \frac{v_i}{v_{\text{Bohm}}} \tag{21}$$

and because we know that the Bohm velocity is $v_{\text{Bohm}} = \sqrt{kT_e/M}$, it is a simple matter to calculate the reduction in the expected flux of ions going to the anode due to the reduction in the Bohm velocity at a given magnetic field strength B. The ion current transverse to the magnetic field between the cusps to the anode is then given by

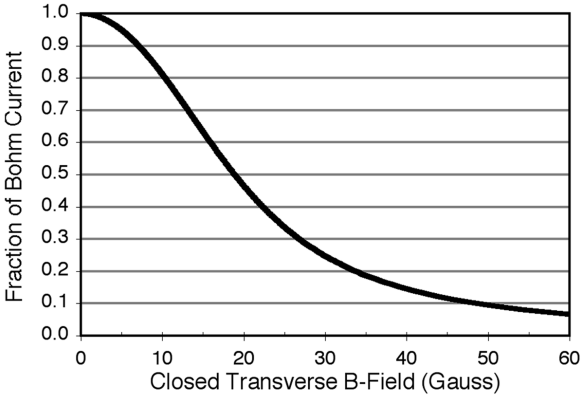

Fig. 8 Ion confinement factor vs closed magnetic field contour value.

$$I_{\text{ia}} = \frac{1}{2}n_i e\sqrt{\frac{kT_e}{M}}A_{\text{as}}f_c \tag{22}$$

where A_{as} is the surface area of the anode exposed to the plasma.

For the case of the NASA Solar Electric Propulsion Technology Applications Readiness (NSTAR) ion thruster [20], the fraction of the Bohm current to the anode ($I_{\text{ia}}/I_{\text{Bohm}} = f_c$) is shown in Fig. 8. We see that at zero transverse magnetic field, the ion flux to the anode is just the Bohm current as expected. As the transverse field reduces the electron mobility, the ions are slowed. In the NSTAR design [20], the last close magnetic contour is about 20 G, and so nearly 50% of the ions initially headed radially toward the anode are lost. For closed magnetic field contours of about 50 G, the ion loss to the anode is reduced by nearly a factor of 10 compared with the unmagnetized Bohm current. The 60 G closed contour in the NEXIS thruster previously shown reduces the ion loss to the anode by nearly a factor of 20. This can make a significant difference in the efficiency of the plasma generator and the amount of discharge power required to produce the beam ions. We see that even though the ions are unmagnetized, ambipolar effects make the multipole magnetic fields very effective in reducing the ion loss to the walls.

D. Plasma and Neutral Parameters in the Discharge Chamber

The ion and excited neutral production rates described by Eqs. (1) and (2) contain the neutral gas density in the discharge chamber. The neutral gas that escapes the chamber (the un-ionized propellant) is the gas injected into the discharge chamber minus the gas particles that are ionized and form the beam

$$Q_{\text{out}} = Q_{\text{in}} - \frac{I_B}{e} \tag{23}$$

The neutral gas that leaks through the grid is the neutral flux on the grids times the grid optical transparency T_a and a conductance reduction term called the Clausing factor:

$$Q_{\text{out}} = \frac{1}{4}n_o v_o A_g T_a \eta_c \tag{24}$$

where v_o is the neutral gas velocity, A_g is the grid area, and η_c is the Clausing factor. The Clausing factor [21] represents the reduced conductance of the grids for multiple grids of finite thicknesses. For typical grid apertures with small thickness to length ratios, the Clausing factor must be calculated using Monte Carlo techniques. In general, ion thruster grids will have Clausing factors on the order of 0.5.

The mass utilization efficiency of the thruster is defined as

$$\eta_m = \frac{I_B}{Q_{\text{in}}e} \tag{25}$$

Equating (23) and (24) and solving for the neutral gas density in the discharge chamber gives

$$n_o = \frac{4Q_{\text{in}}(1-\eta_m)}{v_o A_g T_a \eta_c} = \frac{4I_B}{v_o e A_g T_a \eta_c}\frac{(1-\eta_m)}{\eta_{\text{m}}} \tag{26}$$

The neutral pressure in the discharge chamber P_o during operation of the thruster can be found using this expression and the conversion

$$P_o[\text{torr}] = 1.04\times 10^{-25} n_o\left[\frac{\text{particles}}{\text{m}^3}\right] * T_o[\text{K}] \tag{27}$$

where T_o is the neutral gas temperature in the discharge chamber.

The electron temperature in the discharge chamber can be calculated from particle balance of the ions. The total ion production rate, given by Eq. (1), must equal the total ion loss rate. The ion loss rate can be considered to be the Bohm current in Eq. (9) with the area A representing the sum of all the surfaces A_i that collect ions (cathode, anode, and grids). Because the ion flux to the anode is

reduced by the magnetic field, as discussed in Sec. III.C, the anode area for ion loss can be considered to be $A_a + A_{as} f_c$ in the Bohm current term. Equating (1) and (9), and using Eq. (25) gives

$$\frac{\sqrt{kT_e/M}}{\langle\sigma_i v_e\rangle V + (n_p/n_e)\langle\sigma_i v_p\rangle V} = \frac{2n_o V}{A_i} = \frac{8VQ_{\text{in}}(1-\eta_m)}{v_0 A_g A_i T_a \eta_c} \tag{28}$$

If the total flow into the discharge chamber and the discharge chamber mass utilization efficiency are specified to generate performance curves of discharge loss vs mass utilization efficiency, and the primary electron density calculated, then Eq. (28) can be solved for the electron temperature. This is because the ionization and excitation reaction rate coefficients are functions of the electron temperature, and the rest of the terms on the right-hand side are geometrical. Alternatively, if the beam current is specified, then the right-hand side of Eq. (26) can be used in Eq. (28) to find the electron temperature. Typically, curve fits to the ionization and excitation cross section and reaction rate data from Figs. 5 and 6 are used to evaluate the reaction rate coefficients at a given electron temperature and primary energy in a program that iteratively solves Eq. (27) for the electron temperature.

The primary electron density in Eq. (28) can be evaluated from the primary electron confinement times in the discharge chamber. The emitted current I_e from the hollow cathode is

$$I_e = \frac{n_p e V}{\tau_t} \tag{29}$$

where τ_t is the total primary confinement time that addresses all of the primary electron thermalization and loss mechanisms. The ballistic confinement time for direct primary loss to the anode τ_p was given in Eq. (5). It is assumed that primary electrons that have undergone an inelastic collision with the neutral gas have lost sufficient energy such that they are then rapidly thermalized with the plasma electrons. The mean time for a collision between the primary and a neutral gas atom to occur is given by

$$\tau_c = \frac{1}{n_o \sigma v_p} \tag{30}$$

Using Eq. (26) for the neutral density, the mean collision time is

$$\tau_c = \frac{v_o e A_g T_a \eta_c \eta_m}{4\sigma v_p I_B (1-\eta_m)} = \frac{v_o A_g T_a \eta_c}{4\sigma v_p Q_{\text{in}}(1-\eta_m)} \tag{31}$$

Finally, primary electrons can be thermalized by equilibrating with the plasma electrons. The time for primary electrons to slow into a Maxwellian electron population was derived by Spitzer [22], and is given by

$$\tau_s = \frac{\omega}{2A_D l_f^2 G(l_f \omega)} \tag{32}$$

where $\omega = \sqrt{2V_{\text{pe}}/m}$, eV_{pe} is the primary energy, $l_f = \sqrt{m/2kT_e}$ is the inverse mean velocity of the Maxwellian electrons, A_D is a diffusion constant given by

$$A_D = \frac{8\pi e^4 n_e \ell_n \Lambda}{m^2} \tag{33}$$

and $\ell_n \Lambda$ is the collisionality parameter equal to $23 - \ell_n(n_e^{1/2}/T_e^{3/2})$. The function $G(l_f\omega)$ is defined as

$$G(x) = \frac{\Phi(x) - x\Phi'(x)}{2x^2} \tag{34}$$

and $\Phi(x)$ is the error function:

$$\Phi(x) = \frac{2}{\pi^{1/2}} \int_0^x e^{-y^2}\, dy \tag{35}$$

Spitzer gave the values of $G(x)$ in a table, which is easily fitted so that τ_s can be found as a function of the primary and plasma electron energies.

The total primary electron confinement time can be found from

$$\frac{1}{\tau_t} = \frac{1}{\tau_p} + \frac{1}{\tau_c} + \frac{1}{\tau_s} \tag{36}$$

Some care needs to be used in including the Spitzer slowing time because some ion thruster designs have a very nonmonoenergetic primary energy distribution, which is not described well by Eq. (32).

The current emitted from the hollow cathode is

$$I_e = I_d - I_s - I_k \tag{37}$$

Using Eqs. (29–37), the primary electron density is given by

$$\begin{aligned} n_p &= \frac{I_e \tau_t}{eV} = \frac{I_e}{eV}\left[\frac{1}{\tau_p} + \frac{1}{\tau_c} + \frac{1}{\tau_s}\right]^{-1} \\ &= \frac{I_e}{eV}\left[\frac{v_p A_p}{V} + \frac{4\sigma v_p Q_{\text{in}}(1-\eta_m)}{v_o A_s T_a \eta_c} + \frac{1}{\tau_s}\right]^{-1} \end{aligned} \tag{38}$$

If we assume that the primary electron loss directly to the anode is negligible, the electron equilibration time is long, and the ion current flowing back to the cathode is small, then Eq. (38) can be written as

$$n_p = \frac{I_e v_o A_g T_a \eta_c}{4V\sigma v_p I_B}\frac{\eta_m}{(1-\eta_m)} = \frac{(I_d - I_s) v_o A_g T_a \eta_c}{4V\sigma v_p I_B}\frac{\eta_m}{(1-\eta_m)} \tag{39}$$

This equation demonstrates the characteristic behavior originally described by Brophy [7] of the primary electron density being proportional to the mass utilization efficiency divided by one minus the mass utilization efficiency. This dependence is valid unless there are other paths for the primary electrons to be lost such as ballistically to the anode or by thermalization with the plasma electrons.

E. Power and Energy Balance

The power into the discharge chamber is the emitted current from the hollow cathode times the energy of the electrons into the discharge. The input power is

$$P_{\text{in}} = I_e V_k = I_e(V_d - V_c + V_p + \phi) \tag{40}$$

where V_d is the discharge voltage and ϕ is the plasma potential in the discharge chamber relative to the anode wall. The power into the discharge goes into producing ions, excited neutrals, and Maxwellian electrons. The power from the discharge to the electrodes is from ions flowing to the anode, cathode, and screen plane, and from primary and plasma electrons flowing to the anode. The power out of the discharge is then given by

$$\begin{aligned} P_{\text{out}} = {} & I_p U^+ + I^* U^* + I_s(V_d + V_p + \phi) + I_k(V_d + V_p + \phi) \\ & + (I_B + I_{\text{ia}})(V_p + \phi) + I_a(2T_e + \phi) + I_L(V_d - V_c + V_p + \phi) \end{aligned} \tag{41}$$

where I_p is the total number of ions produced in the discharge, U^+ is the ionization potential of the propellant gas, I^* is the number of excited ions produced in the discharge chamber, U^* is the excitation energy, I_s is the number of ions to the screen grid, I_k is the number of ions flowing back to the cathode, I_B is the beam current, I_a is the plasma electron current to the anode, T_e is the electron temperature, I_{ia} is the ion current to the anode, and I_L is the primary electron fraction lost to the anode. The plasma electron energy lost to the anode wall, given as $2T_e + \phi$ in Eq. (41), is derived in [23].

The emitted current from the hollow cathode I_e was given in Eq. (37), and particle balance at the anode gives

$$I_a = I_d + I_{\text{ia}} - I_L \tag{42}$$

where I_d is the discharge current measured in the discharge power supply. Equating the power into the discharge to the power out, using the particle balance equations [Eqs. (37) and (42)], and solving for the beam current from the thruster gives

$$I_B = \frac{I_d(V_d - V_c + V_p - 2T_e) - I_p U^+ - I^* U^* - (I_s + I_k)(2V_d - V_c + 2V_p + 2\phi) - I_{ia}(V_p + 2T_e + 2\phi) - I_L(V_d - V_c + V_p - 2T_e)}{(V_p + \phi)} \tag{43}$$

The issue in evaluating Eq. (43) for the beam current produced by a given thruster design is that several of the current terms in the denominator contain the plasma density, which is not known. In addition, the beam current I_B is given by the Bohm current averaged over the screen-grid plane times the effective transparency T of the grid

$$I_B = \frac{1}{2} n_i v_a A_g T \approx \frac{1}{2} n_e \sqrt{\frac{kT_e}{M}} A_g T \tag{44}$$

where n_i is the peak ion density at the screen grid, v_a is the ion acoustic velocity, A_g is the active grid area (over which beam is extracted), and T is the effective screen transparency with high voltage applied to the accelerator grids. In this equation, quasi neutrality ($n_i \approx n_e$) is assumed. Equation (44) can be solved for the plasma density using Eq. (43):

$$n_e = \frac{(I_d - I_L)(V_d - V_c + V_p - 2T_e)}{(I_p/n_e)U^+ + (I^*/n_e)U^* + [(1-T)v_a A_g/2](2V_d - V_c + 2V_p + 2\phi) + (v_a A_{as} f_c/2)(V_p + 2T_e + 2\phi)} \tag{45}$$

where the backflowing ion current to the cathode is neglected and the current intercepted by the screen grid I_s is given by

$$I_s = \frac{(1-T)}{2} n_i e v_a A_g \tag{46}$$

We see that the plasma density proportional to the discharge current decreased by the amount of direct primary loss to the anode ($I_d - I_L$), as expected. This is why implementing sufficient cusp magnetic field strength is critical to the thruster performance.

Unfortunately, the ionization and excitation currents in this equation [from Eqs. (1) and (2)] still contain terms proportional to n_p/n_e, so Eq. (45) must be solved parametrically for the plasma density because the other terms except the plasma potential are known from the input parameters and the thruster design. The plasma potential term will be derived in Sec. V. This can be accomplished with simple spreadsheet iterative programs. Once the plasma density is known, the beam current can be calculated from Eq. (44), and the peak plasma density obtained by dividing these results by the flatness parameter for the thruster obtained from probe measurements or two-dimensional codes of the discharge chamber.

F. Discharge Loss

The discharge loss in an ion thruster, neglecting the keeper power, is defined as the total power into the discharge divided by the beam current:

$$\eta_d = \frac{I_d V_d}{I_B} \tag{47}$$

The keeper power is normally small compared with the discharge power, but can easily be added to the numerator of Eq. (47) if desired. Combining Eqs. (43) and (47), the discharge loss is

We can now evaluate the current fractions in this equation. Ions are produced by both the primary electrons from the hollow cathode and by the tail of the Maxwellian distribution of the plasma electrons. The total number of ions produced in the discharge was given in Eq. (1), and the total number of excited neutrals produced in the discharge was given in Eq. (2). Using these equations and Eq. (44) for the beam current, and assuming $n_i \approx n_e$, the first current fraction in Eq. (48) is

$$\frac{I_p}{I_B} = \frac{2n_o n_e e\langle\sigma_i v_e\rangle V}{n_i e\sqrt{(kT_e/M)}A_g T} + \frac{2n_o n_p e\langle\sigma_i v_p\rangle V}{n_i e\sqrt{(kT_e/M)}A_g T} = \frac{2n_o V}{T\sqrt{(kT_e/M)}A_g}\left(\langle\sigma_i v_e\rangle + \frac{n_p}{n_e}\langle\sigma_i v_p\rangle\right) \tag{49}$$

and the second current fraction is likewise

$$\frac{I^*}{I_B} = \frac{2n_o V}{T\sqrt{(kT_e/M)}A_g}\left(\langle\sigma_* v_e\rangle + \frac{n_p}{n_e}\langle\sigma_* v_p\rangle\right) \tag{50}$$

Neglecting the ion current backflowing to the cathode as small, the third current fraction is

$$\frac{I_s}{I_B} = \frac{1-T}{T} \tag{51}$$

The ion current that goes to the anode wall is again the Bohm current reduced by the confinement factor f_c described previously. In this model, the confinement factor for ions to the anode is found from the solution of Eq. (21) evaluated for the particular ion thruster discharge chamber being analyzed. In general for most ion thrusters, if the 50 G contour is closed, it is possible to assume to the first order that $f_c \approx 0.1$ and the ion loss is essentially one-tenth of the local Bohm current headed toward the anode wall. The fourth current fraction in Eq. (48) is then

$$\frac{I_{ia}}{I_B} = \frac{(1/2)n_i e\sqrt{(kT_e/M)}A_{as} f_c}{(1/2)n_i e\sqrt{(kT_e/M)}A_g T} = \frac{A_{as} f_c}{T A_g} \tag{52}$$

where A_{as} is the surface area of the anode facing the plasma in the discharge chamber.

The primary electron current lost to the anode I_L is given by Eq. (3). The last current fraction in Eq. (48) is then

$$\frac{I_L}{I_B} = \frac{n_p e v_p A_p}{(1/2)n_i e v_a A_g T} = \frac{2n_p v_p A_p}{n_e v_a A_g T} \tag{53}$$

The discharge loss can then be written

$$\eta_d = \frac{V_d\{(I_p/I_B)U^+ + (I^*/I_B)U^* + [(I_s + I_k)/I_B](2V_d - V_c + 2V_p + 2\phi) + V_p + \phi + (I_{ia}/I_B)(V_p + 2T_e + 2\phi) + (I_L/I_B)(V_d - V_c + V_p - 2T_e)\}}{V_d - V_c + V_p - 2T_e} \tag{48}$$

$$\eta_d = \frac{V_d\{(I_p/I_B)U^+ + (I^*/I_B)U^* + [(1-T)/T](2V_d - V_c + 2V_p + 2\phi) + (V_p + \phi) + (A_{as}f_c/A_gT)(V_p + 2T_e + 2\phi)\}}{V_d - V_c + V_p - 2T_e} + \frac{V_d[(2n_pv_pA_p/n_ev_aA_gT)(V_d - V_c + V_p - 2T_e)]}{V_d - V_c + V_p - 2T_e} \quad (54)$$

At first glance, it appears that the discharge loss increases directly with the discharge voltage. However, V_d appears in both the numerator and denominator in Eq. (54), and so the direct dependence is weak and increases in V_d increase the primary energy strongly, which increases the ionization rate and beam current. Higher discharge voltages always result in lower discharge losses. Equation (54) illuminates the thruster features that improve the discharge efficiency. Higher screen-grid transparency T, smaller ion confinement factor f_c (better ion confinement), smaller anode area A_a at the cusps all reduce the discharge loss. Lowering the plasma potential also will reduce the discharge loss by reducing the energy lost to the anode by the plasma electrons.

Although the discharge loss in Eq. (54) may appear complicated, it now has a closed form and consists entirely of parameters that are either inputs to the discharge chamber design or operation, or parameters that can be easily calculated. The input data required to evaluate the discharge loss for a ring-cusp thruster are 1) discharge voltage, 2) discharge chamber surface area and volume, 3) magnetic field design (magnetic field at the cusp and the closed contour field between the cusps), 4) grid area and effective transparency, 5) neutral gas temperature in the discharge chamber, and 6) hollow cathode voltage drop.

It is necessary to specify either the discharge current or the beam current to calculate the plasma density in the discharge chamber. The grid transparency is obtained from the grid codes (called "optics codes") such as the Jet Propulsion Laboratory (JPL) CEX-2D ion optics code [24]. The cathode voltage drop is either measured inside the hollow cathode [25], or calculated using a separate two-dimensional hollow cathode plasma models [26].

Discharge chamber behavior is characterized by "performance curves," which are plots of discharge loss vs mass utilization efficiency. These curves provide the electrical cost of producing beam ions as a function of the propellant utilization efficiency, and give useful information of how well the plasma generator works. Performance curves are normally taken at constant beam current and discharge voltage so that the efficiency of producing and delivering ions to the beam is not masked by changes in the discharge voltage or average plasma density at the grids.

IV. Model Predictions

Calculating performance curves (discharge loss vs mass utilization efficiency) using Eq. (54) requires iteration for the solution of electron temperature, discharge current, and/or beam current in the preceding equations. In practice, performance data are produced by varying the discharge current total gas flow and gas flow split between the cathode and main discharge chamber inlets to produce a constant beam current and discharge voltage as the mass utilization efficiency changes. This means that a beam current and mass utilization operating point can be specified, which determines the neutral gas density in the discharge chamber from Eq. (25), and the average plasma density in the discharge chamber from the Bohm current. If an initial discharge current and plasma potential are then specified, the primary electron density can be calculated from Eq. (38) and the electron temperature found from evaluating Eq. (27). These parameters are then used to solve for the discharge loss in Eq. (54). The discharge current and plasma potential are then evaluated from the given discharge voltage and calculated discharge loss. A spreadsheet program in Visual Basic then iterates the model until an electron temperature, discharge current, and plasma potential are found that produces the correct discharge current for the calculated discharge loss at the specified beam current. The solution is relatively insensitive to the plasma potential if the initial choice is reasonably close.

An example of performance curves calculated using this model and compared with measured curves for the NEXIS thruster [10] are shown in Fig. 9. The discharge loss was measured for three different discharge voltages during operation at 4 A of beam current. We see that the model matches the measured the discharge loss well. The 180 eV/ion discharge loss at 26.5 V required that the thruster run at a discharge current of 27.8 A to produce the 4 A of ion beam current. The shape of the performance curves is important. At high mass utilization, the neutral density in the discharge chamber is low and more of the primary energy goes into the plasma electrons and direct loss to the anode. The higher electron temperature increases energy loss to the anode by the plasma electrons and increases the radiation losses by excitation at a fixed beam current. Optimal thruster designs will have flatter discharge performance curves to provide high mass utilization at reasonably low discharge losses.

An important requirement of discharge models for ion thrusters is to handle the primary electrons as correctly as possible. For the case addressed here of monoenergetic primaries, the primary density is determined by collisional (electron–neutral and electron–electron) and ballistic (direct–anode) losses that change as a function of the neutral pressure. If primary electrons are neglected altogether (assumed thermalized immediately in the cathode plume) so that the plasma is produced only by ionization by the tail of the Maxwellian electron population, the discharge loss is extremely high. This is shown in Fig. 10, where the discharge loss increases to over 300 eV/ion at high mass utilization efficiency if the primary electrons are neglected entirely. Likewise, if the primary electron density is assumed to be constant and independent of the neutral pressure, then the discharge loss curve in Fig. 10 has a steep slope resulting from excessive primary density and ionization at high pressures (low mass utilization). Clearly, correct handling of the primary electron generation and loss rates is important. In reality, the primary electrons have a spread in energy and are better represented by a non-Maxwellian distribution, which will not be covered in this paper.

Having a representative model of the discharge permits environmental changes to the thruster to be understood. For example, the neutral gas temperature depends on the operating time of the thruster until equilibrium is reached, which can take hours in some cases. The 0-D discharge chamber model accurately showed

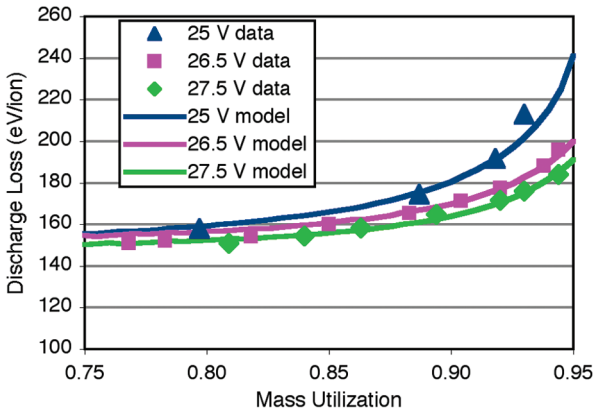

Fig. 9 Discharge loss vs mass utilization efficiency in the NEXIS thruster, where the symbols are data and the solid curves are model predictions.

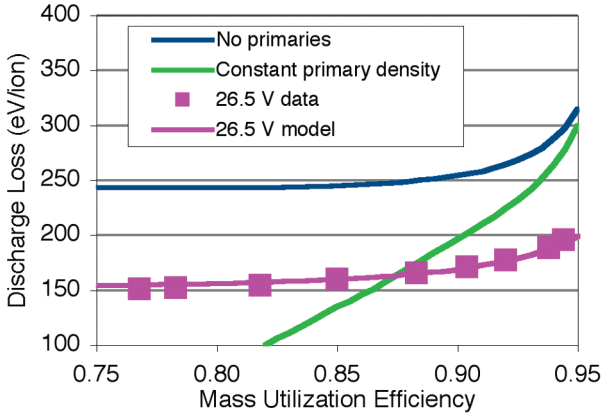

Fig. 10 Discharge loss predictions for the cases of no primary electrons and a constant primary electron density.

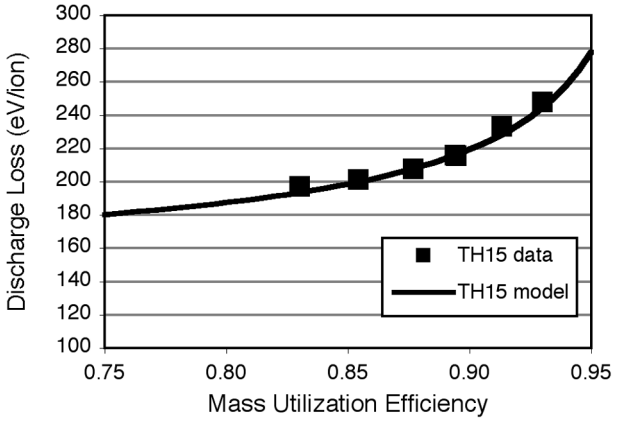

Fig. 11 Discharge loss vs mass utilization efficiency for the NSTAR thruster [20] at the high power TH15 throttle point.

the change in discharge loss as the NEXIS thruster heated up after turn-on based on the change in the neutral gas temperature [10]. This effect reduces the neutral density in the discharge chamber at a given input rate, which increases the primary losses to the anode and raises the electron temperature, which also increases the electron convection losses. A similar effect is observed as the grids erode with time in that the pressure drops in the discharge chamber, and the discharge performance degrades because of the same higher loss mechanisms.

The discharge model works well on other thrusters. Figure 11 shows the discharge loss measured at JPL for a laboratory copy of the NSTAR thruster [27] operating at the full power (2.3 kW) TH15 throttle level. The model predictions agree very well with the thruster data using the measured [28] 6.5 V cathode voltage drop in the NSTAR hollow cathode. Figure 12 shows the discharge loss as a function of the mass utilization efficiency reported recently for the NASA Evolutionary Xenon Thruster (NEXT) EM3 [29], which is presently undergoing a long duration test (LDT) at NASA Glenn Research Center. The data shows the performance at three of NEXT throttle points, and the model results agree well with the data if the hollow cathode voltage drop (V_c) input to the model is assumed to increase as the discharge current decreases. This behavior of the cathode voltage drop changing inversely with discharge current has been reported [25,28] in measurements on a similar but slightly larger cathode, and is consistent with a cathode self-heating model [30] where higher resistive drops are required to sustain the cathode temperature as the discharge current drops. Similar good agreement between the model predictions and unpublished thruster performance data is obtained with the XIPS ion thruster [2].

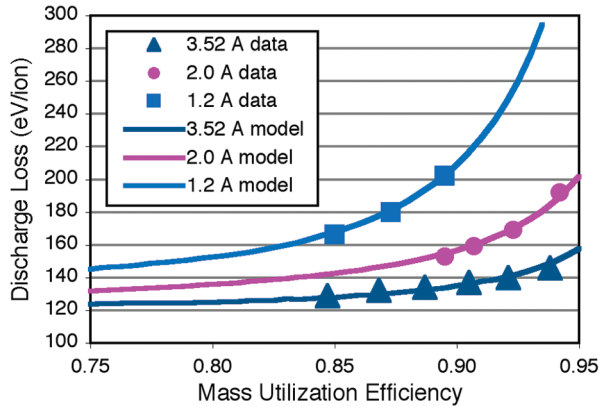

Fig. 12 Discharge loss vs mass utilization efficiency for the NEXT thruster [29] at three of its throttle points.

V. Discharge Stability

There is a strong relationship between the discharge loss and the stability of the discharge [9]. We saw from inspection of Eq. (54) that the efficiency increases if the anode area for primary electron loss is minimized. Although it is logical to assume that this is also true if the anode area for plasma electrons is minimized to reduce the energy loss due to the Maxwellian population, a dependence on A_a does not appear in Eq. (54). However, because the discharge current is carried primarily by the plasma electrons, the sheath potential at the anode given in Eq. (8) is found to decrease as the anode area decreases for a given discharge current. The sheath potential dependence is contained in the discharge loss equation, which suggests that minimizing the sheath potential maximizes the efficiency [9]. However, the anode area for plasma electrons cannot go to zero because the discharge current could not be collected by the anode and the discharge would either interrupt or go unstable. Therefore, there is a minimum anode area and plasma potential for both efficiency and stability, which must be determined.

The value of the plasma potential relative to the anode (the anode sheath voltage drop) can be calculated using Eq. (8). The electron current to the anode at the cusp is found from Eq. (42). Using Eqs. (3), (8), and (21) and dividing by the beam current in Eq. (9), Eq. (42) becomes

$$\frac{I_d}{I_B} + \frac{(1/2)n_e e v_a A_{\text{as}} f_c}{(1/2)n_e e v_a A_g T} - \frac{n_p e v_p A_p}{(1/2)n_e e v_a A_g T} = \frac{(1/4)(8kT_e/\pi m)^{1/2} e n_e A_a}{(1/2)n_e e v_a A_g T} \exp^{-e\phi/kT_e} \tag{55}$$

Solving for the plasma potential gives

$$\phi = \frac{kT_e}{e} \ell_n \left(\frac{(2M/\pi m)^{1/2}(A_a/A_g T)}{(I_d/I_B) + (A_{\text{as}} f_c/A_g T) - (2n_p v_p A_p/n_e v_a A_g T)} \right) \tag{56}$$

As seen in Eq. (56), as the anode area decreases, the plasma potential goes down. If the anode area is made too small, then the plasma potential will go negative relative to the anode potential. This produces a so-called positive-going (or electron accelerating) anode sheath, as illustrated in Fig. 13. In this case, the anode area available is insufficient to collect the total discharge current by collection of the entire incident random electron flux on the total cusp area. The plasma then biases itself to pull in electrons in the Maxwellian distribution that are not headed toward the anode, which delivers more current to satisfy the charge balance requirement. However, once the potential goes sufficiently negative relative to the anode to repel the ions (about T_i), then the anode area for the plasma electron is not the hybrid area, but just twice the plasma electron Larmor radius times the cusp length, similar to Eq. (4) for the primary loss area. This results in a significant decrease in the cusp anode area, further lowering the plasma potential relative to the anode. Examining the

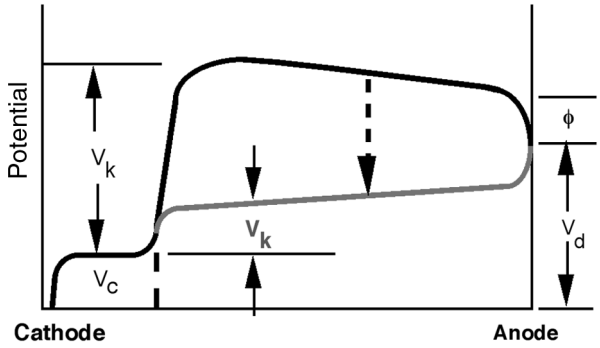

Fig. 13 Plasma potential vs cusp magnetic field strength for a thruster design with four and six magnet rings.

potential distribution in the plasma in Fig. 13, we see that the positive-going anode sheath will subtract from the primary electron energy V_k by transferring the energy into the anode by electron acceleration. The ionization rate then decreases, and the discharge collapses into a high impedance mode or oscillates between this mode and a positive potential typically on power supply time constants as the supply tries to reestablish the discharge by increasing the anode voltage.

The stability of the plasma discharge at a given operating point (discharge current, beam current, pressure, etc.) is therefore determined by the magnetic field design. For example, in Fig. 14, the 0-D model predicts that a four-ring design of a strawman thruster would be unstable (when the potential goes negative relative to the anode) for cusp magnetic fields greater than 2100 G. Because strong magnetic fields are desirable from a primary electron and ion confinement point of view, additional rings are required to maintain a positive plasma potential for stability. A six-ring design increased the anode area sufficiently to raise the plasma potential at the 2000 G magnet design point. This came at some loss of efficiency, which appears to always be the tradeoff.

Finally, the 0-D model predicted the correct magnetic field design for stability at the desired operating point, but the discharge was found to go unstable (oscillate) during recycles. In a recycle, the high voltage is turned off momentarily (typically 0.05–0.5 s) to clear a high voltage breakdown somewhere in the thruster grids or body. Without high voltage on, ions that would have left the discharge chamber as beam ions now tend to strike the accelerator grid and backflow into the discharge chamber as neutrals. This raises the neutral gas pressure in the discharge chamber, which has two effects. First, the higher neutral pressure then tends to collisionally thermalize the primary electrons more rapidly, which can lead to a reduction in the plasma potential [9]. Second, it is standard to reduce the discharge current during the recycle to reduce the ion current bombarding the accel grid and make it easier to restart the engine by limiting the amount of positive charge in the grid gaps that the power supplies must conduct during restart to reestablish the high voltage. Lowering the discharge current while raising the neutral pressure leads to a lower impedance discharge and a lower discharge voltage. This effect also contributes reducing the plasma potential.

We can calculate the time dependent behavior of the pressure in the discharge chamber from the high-voltage-off event using molecular dynamics, and evaluate the subsequent time dependent plasma potential for stability from the 0-D model. The time dependent pressure in the thruster is given by

$$V\frac{dP}{dt} = Q_{\text{in}} - C\Delta P \tag{57}$$

where V is the discharge chamber volume, P is the pressure in the thruster discharge chamber, C is the conductance of the grids, and ΔP is the pressure drop across the grids. The initial pressure just before the start of the recycle when the thruster is operating normally is found from Eqs. (25) and (26):

$$P_o = 4.1 \times 10^{-25}\frac{T_o Q_{\text{in}}(1-\eta_m)}{v_o e A_g T_a \eta_c} \tag{58}$$

With the high-voltage off, the ions and neutrals flow to the grid region, where a fraction exits through the accel aperture and escape, and the remainder strikes the upstream side of the grids and flows back into the thruster. Because the grid conductance is defined as the flow divided by the pressure drop [31], the final pressure after steady state has been achieved is

$$P_f = (1-T_a)\frac{Q_{\text{in}}}{C} \tag{59}$$

where the downstream pressure from the grids has been neglected as small. The conductance of the grids can be estimated from the molecular conductance of a thin aperture [31] times the Clausing factor [23] for the finite thickness grids. The conductance is then

$$C = 3.64\left(\frac{T}{M_a}\right)^{1/2} T_a A_g \eta_c,\ \text{l/s} \tag{60}$$

where M_a is the ion mass in atomic mass units (amu), and the effective open area of the grids is the optical transparency of the accel grid T_a times the grid area A_g. Integrating Eq. (57) from the initial pressure to the final pressure gives

$$P(t) = P_f - (P_f - P_o)e^{-t/\tau_g} \tag{61}$$

where $\tau_g = V/C$ is the gas flow time constant for filling the thruster chamber. Because we are using Eq. (55) to find the final pressure, the gas flow rate has to be converted from particles per second to torr · l/s by multiplying the flow by a constant given by 2.81×10^{-20}.

Figure 15 shows an example of the pressure increase with time in the NEXIS thruster discharge chamber from the start of a recycle.

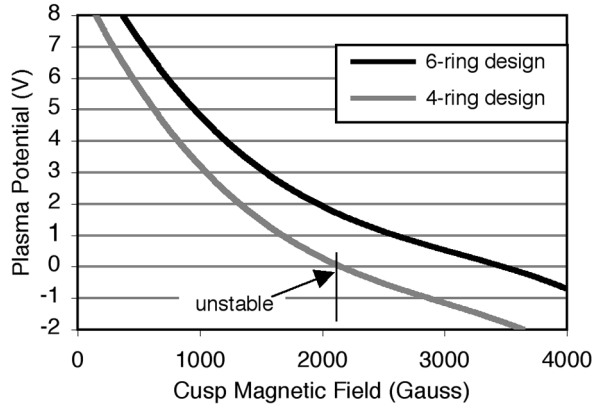

Fig. 14 Plasma potential vs cusp magnetic field strength at the anode wall for a thruster design with four and six magnet rings.

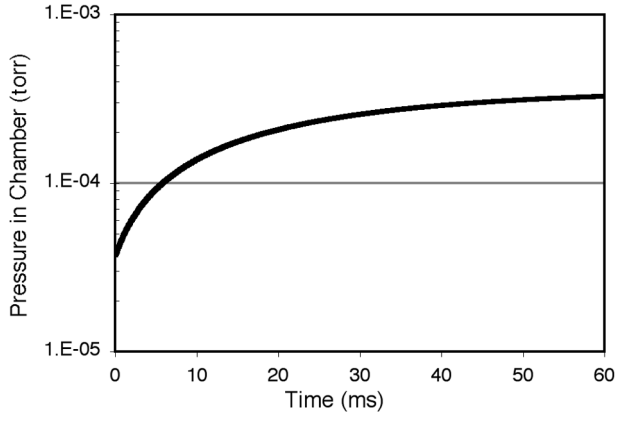

Fig. 15 Example of the pressure rise in the NEXIS thruster calculated during a recycle.

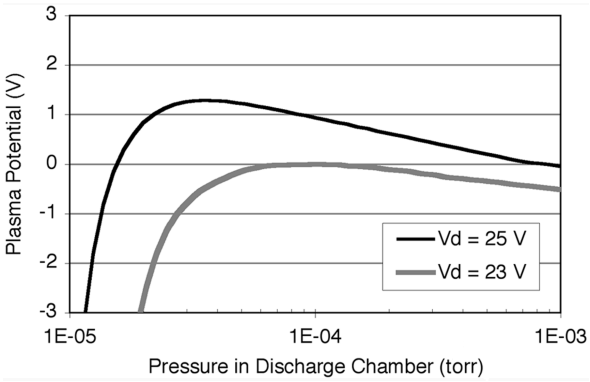

Fig. 16 Plasma potential as a function of pressure inside the discharge chamber for two different discharge voltages.

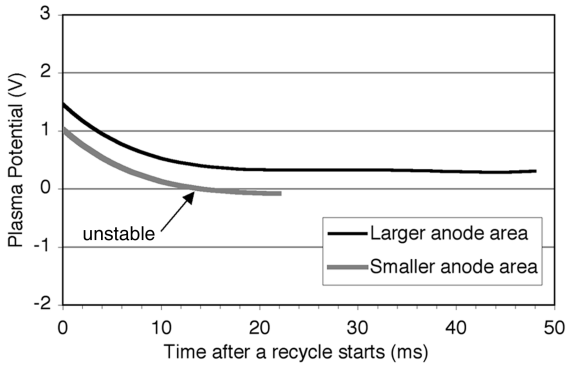

Fig. 17 Plasma potential vs time showing instability onset and anode area increase stabilization.

The pressure in the discharge chamber during normal operation is in the mid-10^{-5} torr range due to the large grid area and high mass utilization efficiency. The pressure in the discharge chamber reaches equilibrium in about 60 ms, with the pressure increasing by almost an order of magnitude once the high voltage is turned off. This factor of 10 pressure rise is consistent with >90% mass utilization efficiency of the NEXIS thruster during beam extraction.

The plasma potential responds to the pressure increase in the discharge chamber due to the changes in the electron temperature, primary electron density, and grid transparency. The plasma potential tends to have a maximum at a given pressure [9], and decrease at higher and lower pressures. This is shown in Fig. 16 for two discharge voltages in a given thruster design. During the recycle, the discharge voltage tends to decrease due to the higher pressure in the discharge chamber increasing the ionization rate, and again because the discharge current is usually reduced (called cutback) to aid turning the thruster back on. If the discharge voltage stayed at the nominal 25 V in this example, Fig. 16 shows that the plasma potential would only go negative at pressures approaching 10^{-3} torr, which, according to Fig. 15, this thruster does not experience. However, the cutback condition with lower discharge currents also reduces the discharge voltage, which contributes to a further reduction in the plasma potential. The combination of high pressure and lower discharge voltage drives the plasma potential negative, which causes the discharge to go unstable.

The model shows that recycle instabilities are a voltage effect, not a current effect. A thruster design that produces a stable discharge under normal conditions can go unstable due to negative plasma potentials as the pressure rises and the discharge voltage decreases. The plasma potential for two different magnet designs is shown in Fig. 17, illustrating the effect of a smaller anode area at a given pressure. Increasing the anode area increases the plasma potential at a given pressure, which permits the discharge current during the recycle to be cutback to the desired level without oscillating. Of course, implementing a larger anode area increases the anode-loss in the discharge chamber and raises the discharge loss. A tradeoff between good performance and stable operation during recycling must then made in the design of the thruster discharge chamber.

VI. Conclusions

The self-consistent discharge plasma model described here provides good agreement with the experimental discharge performance data and a predictive capability for ion thruster performance. Although 0-D models like this can provide very good information on the design parameters of thrusters and can predict their performance reasonably well, there are several limitations to their use. First, the model assumes a uniform neutral gas and plasma density and averages the ion production and loss throughout the volume of the discharge chamber. For ion thrusters with significantly nonuniform plasmas, such as NSTAR [20], this can lead to some inaccuracies especially at high mass utilization efficiencies where the double ion production is high on axis. In addition, because the source of the gas is from both the localized hollow cathode aperture and the gas manifold inside the discharge chamber, the neutral density is also not uniform. These issues, along with the problem of dispersing the cathode plume, have to be modeled by full two-dimensional discharge chamber codes such as developed by Wirz and Katz [32]. However, simple 0-D models such as this get you over 90% of the way there, and are very useful in understanding ion thruster performance and behavior as operation parameters are changed or the thruster wears toward end of life.

Acknowledgment

The research described here was carried out at the Jet Propulsion Laboratory, California Institute of Technology.

References

[1] Brophy, J. R., Brinza, D. E., Polk, J. E., Henry, M., Sengupta, A., "DS1 Hyper-Extended Mission," AIAA Paper 2002-3673, 2002.

[2] Goebel, D. M., Martinez-Lavin, M., Bond, T. A., and King, A. M., "Performance of XIPS Electric Propulsion in Station Keeping of the Boeing 702 Spacecraft," *38th Joint Propulsion Conference*, AIAA Paper 2002-5117, 2002.

[3] Kaufman, H. R., "Ion Rocket with an Electron-Bombardment Ion Source," NASA TN-D-585, 1961.

[4] Masek, T. D., "Plasma Properties and Performance of Mercury Ion Thrusters," *AIAA Journal*, Vol. 9, No. 2, Feb. 1971, pp. 205–212.

[5] Ward, J., Masek, T., "Discharge Computer Model for an Electron Bombardment Thruster," AIAA Paper 76-1009, 1976.

[6] Matossian, J. N., and Beattie, J. R., "Model for Computing Volume Averaged Plasma Properties in Electron-Bambardment Ion Thrusters," *Journal of Propulsion and Power*, Vol. 5, No. 2, March–April 1989, pp. 188–196.

[7] Brophy, J. R., "Ion Thruster Performance Model," NASA CR-174810; Ph.D. Thesis, Colorado State Univ., Fort Collins, CO, Dec. 1984.

[8] Goebel, D. M., Polk, J. E., and Sengupta, A., "Discharge Chamber Performance of the NEXIS Ion Thruster," *40th AIAA Joint Propulsion Conference*, AIAA Paper 2004-3813, 2004.

[9] Goebel, D. M., "Ion Source Discharge Performance and Stability," *Physics of Fluids*, Vol. 25, No. 6, June 1982, p. 1093.

[10] Polk, J., Goebel, D. M., Snyder, J. S., Schneider, A. C., Johnson, L., and Sengupta, A., "Performance and Wear Test Restuls for a 20-kW-Class Ion Engine with Carbon-Carbon Grids," *41th AIAA Joint Propulsion Conference*, AIAA Paper 2005-4393, 2005.

[11] Randolph, T., and Polk, J., "Overview of the Nuclear Electric Xenon Ion System (NEXIS) Activity," *40th AIAA Joint Propulsion Conference*, AIAA Paper 2004-3450, 2004.

[12] Hayakawa, Y., Miyazaki, K., and Kitamura, S., "Measurements of Electron Energy Distributions in a 14-cm Diameter Ring Cusp Ion Thruster," *Journal of Propulsion and Power*, Vol. 8, No. 1, Jan.–Feb. 1992, pp. 118–126.

[13] Herman, D. A., and Gallimore, A. D., "Discharge Cathode Electron Energy Distribution Functions in a 40-cm NEXT-type Ion Engine," *41st Joint Propulsion Conference*, AIAA Paper 2005-4252, 2005.

[14] Rapp, D., and Englander-Golden, P., "Total Cross Sections for Ionization and Attachment in Gases by Electron Impact, 1: Positive Ionization," *Journal of Chemical Physics*, Vol. 43, No. 5, 1965, pp. 1464–1479.

[15] Hayashi, M., "Determination of Electron-Xenon Total Excitation Cross-Sections, from Threshold to 100-eV, from Experimental Values of Townsend's α," *Journal of Physics D: Applied Physics*, Vol. 16, No. 4, 1983, pp. 581–589.

[16] Leung, K., Hershkowitz, N., and MacKenzie, K., "Plasma Confinement By Localized Cusps," *Physics of Fluids*, Vol. 19, No. 7, July 1976, pp. 1045–1053.

[17] Bohm, D., *Characteristics of Electric Discharges in Magnetic Fields*, edited by Guthrie, A., and Wakerling, R., McGraw–Hill, New York, 1949, pp. 1–76.

[18] Chen, F. F., *Introduction to Plasma Physics and Controlled Fusion*, Vol. 1, Plenum, New York, 1984.

[19] Book, D., *NRL Plasma Formulary*, Naval Research Lab., Washington, D.C., 1998.

[20] Brophy, J. R., "NASA's Deep Space 1 Ion Engine," *Review of Scientific Instruments*, Vol. 73, No. 2, Feb. 2002, pp. 1071–1078.

[21] Clausing, P., "Flow of Highly Rarefied Gases Through Tubes of Arbitrary Length," *Journal of Vacuum Science and Technology*, Vol. 8, No. 5, Sept. 1971, pp. 636–646.

[22] Spitzer, L., *Physics of Fully Ionized Gases*, Interscience, New York, 1956, p. 80.

[23] Divergilio, W., Goede, H., and Fosnight, V., "High Frequency Plasma Generators for Ion Thrusters," NASA Interim Rept. CR-167957, Nov. 1981.

[24] Anderson, J. J., Katz, I., and Goebel, D., "Numerical Simulation of Two-Grid Ion Optics Using a 3D Code," *40th Joint Propulsion Conference*, AIAA Paper 2004-3782, 2004.

[25] Goebel, D. M., Jameson, K., Watkins, R., and Katz, I., "Cathode and Keeper Plasma Measurements Using an Ultra-Fast Miniature Scanning Probe," *40th Joint Propulsion Conference*, AIAA Paper 2004-3430, 2004.

[26] Mikellides, I., Katz, I., Goebel, D. M., and Polk, J., "Theoretical Model of a Hollow Cathode Insert Plasma," AIAA Paper 2004-3817, 2004.

[27] Sengupta, A.,"Experimental Investigation of Discharge Plasma Magnetic Confinement in an NSTAR Ion Thruster," *41th AIAA Joint Propulsion Conference*, AIAA Paper 2005-4069, 2005.

[28] Jameson, K. K., Goebel, D. M., and Watkins, R. M., "Hollow Cathode and Keeper-Region Plasma Measurements," *41th AIAA Joint Propulsion Conference*, AIAA Paper 2005-3667, 2005.

[29] Frandina, M., Arrington, L., Soulas, G. C., Hickman, T., and Patterson, M. J., "Status of the NEXT Ion Thruster Long Duration Test," *41th AIAA Joint Propulsion Conference*, AIAA Paper 2005-4065, 2005.

[30] Katz, I., Polk, J., Mikellides, I., Goebel, D., and Hornbeck, S., "Combined Plasma and Thermal Hollow Cathode Insert Model," *International Electric Propulsion Conference*, International Electric Propulsion Conference Paper 2005-228, 2005.

[31] Lewin, G., *Fundamentals of Vacuum Science and Technology*, McGraw–Hill, New York, 1965.

[32] Wirz, R., and Katz, I., "Plasma Processes in DC Ion Thruster Discharge Chambers," *41th AIAA Joint Propulsion Conference*, AIAA Paper 2005-3690, , 2005.

A. Gallimore
Associate Editor